Sensors and Materials, Vol. 36, No. 6 (2024) 2597–2612
MYU Tokyo

S & M 3689

Fault Diagnosis of Permanent Magnet Synchronous Motor Based on 1D-Convolutional Neural Network

Meng-Hui Wang, Fu-Chieh Chan, and Shiue-Der Lu*

Department of Electrical Engineering, National Chin-Yi University of Technology,
57, Sec. 2, Chung Shan Rd., Taiping Dist., Taichung 41170, Taiwan (R.O.C.)

(Received December 18, 2023; accepted May 30, 2024)

Keywords: 1D convolutional neural network (1D-CNN), permanent magnet synchronous motor (PMSM), motor fault diagnosis

In this study, we applied 1D convolutional neural networks (1D-CNNs) to permanent magnet synchronous motor (PMSM) fault diagnosis on 12 common PMSM fault types, namely, normal motor (Class A), poor dynamic balance of rotor (Class B), bent shaft (Class C), magnet demagnetization (Class D), uneven air gap (Class E), rotor misalignment (Class F), stator coil three-phase imbalance (Class G), stator coil layer short circuit (Class H), poor lubrication of bearing (Class I), damaged inner ring of bearing (Class J), damaged bearing ball (Class K), and poor assembly (Class L). First, a vibration spectrum analyzer was used to measure and capture the vibration signals of a faulty motor. Then, the 1D-CNN was utilized to analyze and diagnose the captured data. The results showed that the proposed 1D-CNN method can identify 11 motor fault types with an accuracy of up to 99.7%, higher than the 96.1% accuracy of 2D convolutional neural networks (2D-CNNs). In addition, the fault diagnosis system developed in this study can perform a rapid motor fault diagnosis with a small amount of training data, significantly reducing the detection cost for PMSM fault diagnosis.

1. Introduction

The permanent magnet synchronous motor (PMSM) has advantages of low noise, high efficiency, small size, and light weight. It is replacing traditional permanent magnet DC brushed and induction motors. It is widely used in national defense technology, aerospace, machine tools, industrial automation, and electric vehicles.[1,2] At present, instruments are used to identify motor fault types, which are then analyzed by professionals to identify the cause of the observed abnormality. Human evaluation results differ owing to differences in knowledge, experience, and analysis methods. This traditional troubleshooting method may lead to errors in judgment and unnecessary waste of human resources and time.[3]

The numerous and complex types of motor fault[4,5] can be divided into stator, rotor, and bearing faults. A bearing is an important part of rotating machinery. It supports mechanical rotation and has high precision requirements. A bearing fault is a common motor fault type,

*Corresponding author: e-mail: sdl@ncut.edu.tw
https://doi.org/10.18494/SAM4834

ISSN 0914-4935

often accompanied by sound and vibrations.[6–10] Once a bearing fault is detected and the bearing is not changed on time, the equipment may be damaged or even scrapped, causing heavy losses of property.[11,12]

Guesmi *et al.* used the motor stator current waveform to diagnose fault types, such as uneven air gap, bearing fault, and induction motor rotor bar breakage.[13] Huang *et al.* used motor vibration signals as analytical data and an extension neural network (ENN) for induction motor fault diagnosis.[14] Convolutional neural networks (CNNs) have been extensively used owing to their strong ability to extract features from various types of complex information and outstanding characteristics. Related research involved face recognition,[15] target tracking,[16] target diagnosis,[17] and time-frequency analysis.[18] In a fault diagnosis system based on 1D-CNN and multi-sensor information fusion,[19] the data from seven motor states were captured for training, testing, and verification. The results showed that the fault diagnosis accuracy of the model was 99.3%. Zhou *et al.* built a fault diagnosis model based on CNN.[20] They used speed signals of a faulty bearing at different rotational speeds for model training and testing. The accuracy of the model was as high as 98.7%. Özcan *et al.* proposed an enhanced bearing fault diagnosis system based on a multi-channel and multi-level 1D-CNN classifier.[21] The classifier processed the vibration data collected from multiple accelerometers mounted on test bench bearings and applied them to the intermediate shaft bearing vibration dataset of the inner ring and rolling element faults. A multi-head 1D-CNN method used two accelerometers measuring in different directions to detect and diagnose normal motors and six types of fault in electric motors.[22] The proposed method was verified by experiments involving seven types of induction fault and operating conditions. The results showed that the proposed architecture was accurate for vibration signal measurement data and multi-sensor fault detection using time series.

This study is based on the real fault data of 12 types of motor, namely, normal motor (Class A) and 11 fault types (Classes B to L). With vibration signal measurement data using time series, training and validation models were built using 1D-CNN. These models can be applied to front-line work sites without building an online monitoring system. This simple model covers a wide range of faults with an accuracy of 99.7%.

2. Overall System Architecture

2.1 Test platform

The vibration spectrum analyzer converts physical quantities such as displacement, speed, and acceleration of machine vibration into voltage, charge, and current signals. Afterwards, these signals are amplified, and fast Fourier transform (FFT) is used to analyze the obtained spectra. In this study, the HJ-4250S vibration spectrum analyzer (G-Tech Corp) was utilized[23] as the testing equipment. In Fig. 1, the test platform is shown to include a dynamic signal FFT analyzer, an optical tachometer, a high-sensitivity force gauge, a vibration sensor, PMSM, and a frequency converter to drive the motor.

The design specifications of the PMSM used in this study are shown in Table 1. The same frequency converter was used to drive all test motors to eliminate the possible effects of different driving controllers.

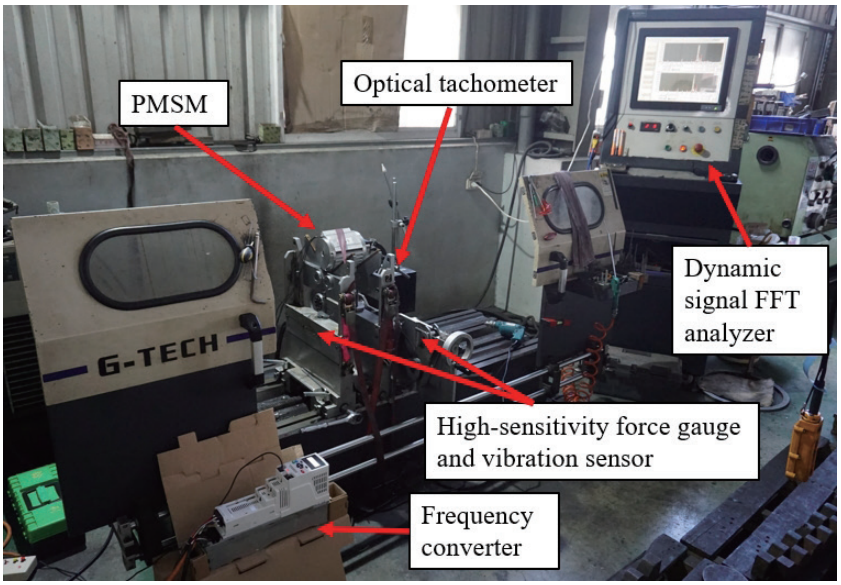

Fig. 1. (Color online) Photograph of frequency spectrum analyzer and related equipment.

Table 1
Prototype design specifications.

Item	Specification
Motor type	IPM-BLDC Motor
Poles/slots	4 Poles/24 Slots
Rated voltage	311 VDC
Rated rpm	2500 rpm
Rated power	600 W
Phase	Three-phase
Construction of winding/connection	Single layer concentric winding/Y-connection

2.2 Motor fault types

The motor manufacturing process consists of multiple procedures. In this study, 11 common motor fault types were proposed and divided into four major classes, namely, rotor, stator, bearing, and assembly. The assembly fault is a motor abnormality type most likely to be ignored in practice. When all parts are normal, motor abnormalities may occur owing to differences in assembly sequence and technique used. This type of motor fault was added to improve the motor fault identification system. The rotor, stator, and bearing faults are detailed below.

2.2.1 Rotor faults

2.2.1.1 Poor dynamic balance of rotor

The rotor goes through a dynamic balancing process in the motor manufacturing process. The dynamic balancing methods include deweighting and weighting methods, and the weighting

method was adopted in this study. As shown in Fig. 2(a), the rotor of a normal motor is on the rotor silicon steel sheet, not exceeding the outer diameter range of the rotor. It is balanced by filling clay or glue. Figure 2(b) shows the poor dynamic balance of the motor's rotor, and there is no dynamic balance processing on both sides of the rotor.

2.2.1.2 Bent shaft

The fault of rotating shaft bending is mostly induced by external force. In this study, we used a certified vernier caliper to measure the distance between the rotating shaft's top plane and the motor's front cover. The H class test standard of the International Organization for Standardization (No. ISO 2768-1, 2:1989) suggests/mandates that the measurement data must be 50 mm and the tolerance is ±0.05 mm.[24] In Fig. 3(a), if the distances on both sides are the same and within the tolerance, it is a normal motor, whereas in Fig. 3(b), if the shaft is bent, the distance from different positions on the front plane to the front end of the shaft will be significantly different.

2.2.1.3 Magnet demagnetization

The partial demagnetization abnormality of the magnet may be induced by high-temperature demagnetization, instant strong magnetic field impact, external impact, and material problems during magnet production. In this study, the Gauss meter tester (American Sypris Corp. F.W. BELL Model 6010) was used as the inspection equipment.[25] According to the inspection standards provided by the magnet manufacturer, when measuring 360° of the magnets attached to the rotor, the maximum magnetic flux should be 4000 (Gs) and the minimum value should be 2000 (Gs) with an error of ±5%. Figures 4(a) and 4(b) show the magnetic flux measurement

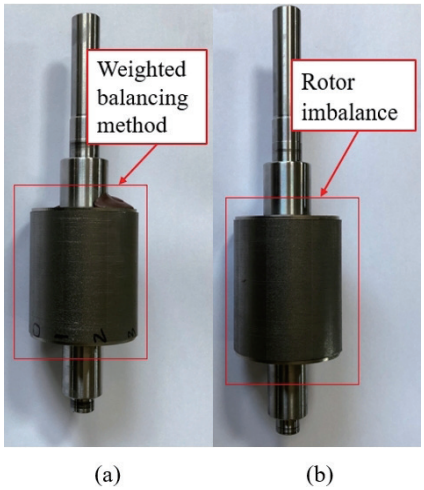

Fig. 2. (Color online) Photographs of (a) normal rotor with dynamic balance and (b) abnormal rotor with poor dynamic balance.

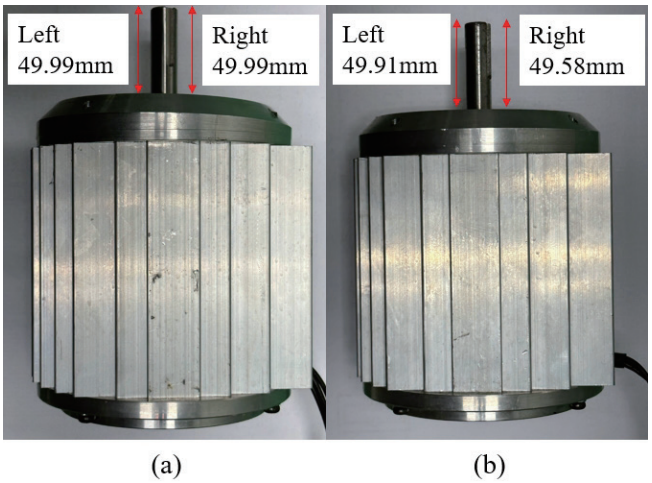

Fig. 3. (Color online) Photographs of (a) normal motor and (b) motor with bent shaft.

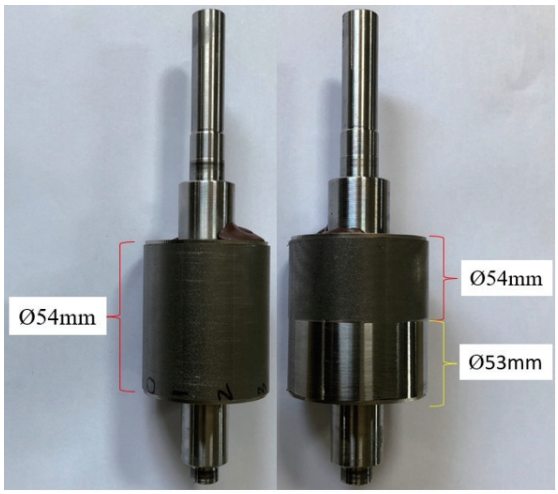

Fig. 4. (Color online) Magnetic flux measurement results of (a) normal motor and (b) faulty motor with partial demagnetization.

results of a normal motor and a faulty motor with partial demagnetization, respectively. The minimum value is only 1137 (Gs), which is identified as the partial demagnetization of the magnet.

2.2.1.4 Uneven air gap

If the outer diameter of the rotor is processed without positive attention, it may induce the motor abnormality of an uneven air gap. In Fig. 5(a), in the same rotor, the outer diameter of the rotor silicon steel sheet is shown to be ψ54 mm, which is characteristic of a normal motor. In Fig. 5(b), the outer diameters of the upper red and lower yellow areas are ψ54 and ψ53 mm, respectively. The air gap after assembly has a difference of 0.5 mm, which is an uneven rotor air gap type.

2.2.1.5 Rotor misalignment

The rotor misalignment mainly resulted from the poor positioning of the rotor silicon steel sheet during press-fitting, which induced the rotor and stator misalignment inside the motor. In Fig. 6, the one on the left is the rotor of the faulty motor and the one on the right is the normal motor rotor. The rotor position deviation between them is 4.5 mm.

2.2.2 Stator faults

2.2.2.1 Stator coil three-phase imbalance

The faults often occur in the manufacturing of the finished stator. Owing to the inconsistent number of turns or wire diameters of the three sets of coils with different phases, the line

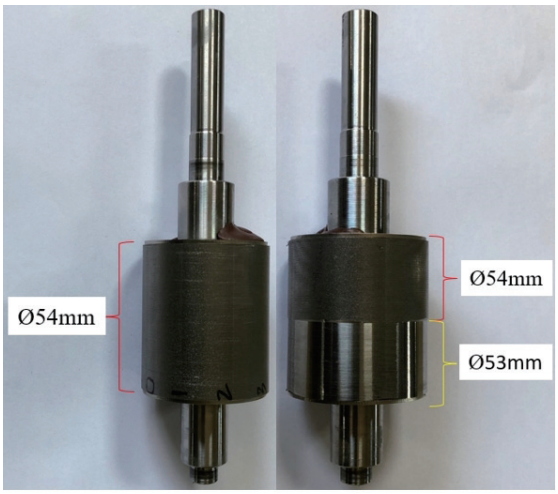

Fig. 5. (Color online) Photographs of (a) normal rotor with even air gap and (b) abnormal rotor with uneven air gap.

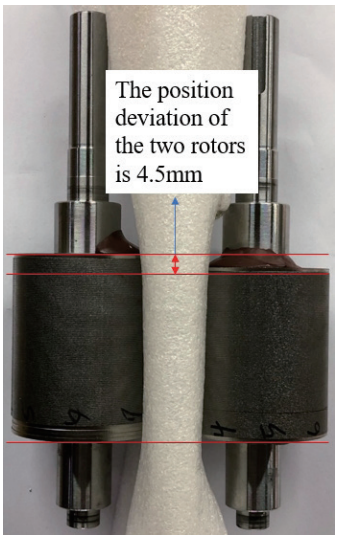

Fig. 6. (Color online) Comparison photos of faulty and normal rotosr in terms of rotor misalignment.

resistance among the three phases is unbalanced. In this study, we used the RM3544-01 micro-ohmmeter tester (Japan HIOKI Corp.) as the inspection equipment.[26] The inspection standard is to measure the motor's line resistance in the same environment. According to the inspection standards in the Electrical Equipment Engineering Management Practice of the Public Construction Committee of the Executive Yuan of the Republic of China, the difference in line resistance between different sets of coils in the same motor should be less than 3%;[27] otherwise, it is identified as a fault. Figures 7(a) and 7(b) show the same motor, and the line resistances (U–V and U–W phases) are similar. The stator coil three-phase balance is determined if the two values are similar. Figures 7(c) and 7(d) show the same faulty motor, but the line resistances (U–V and U–W phases) are different. If the difference between the two values is greater than 3%, it is identified as the abnormality of stator coil three-phase unbalance.

2.2.2.2 Stator coil layer short circuit

The short circuit of the stator coil layer is an abnormal condition that is difficult to find. It occurs mainly because the insulation layer between coils is damaged during production. We used the DWX-05A pulse coil tester (Japan KOKUSAI Corp.) as the inspection equipment.[28] The detection method measures the normal motor's current waveform and then compares it with the current waveform of the motor to be tested. It makes a judgment based on the waveform area ratio and waveform area difference ratio. As shown in Figs. 8(a) and 8(b), the criterion of waveform area ratio is 10%. The waveform area difference ratio (Dif-A) is 10%, and the test values in Fig. 8(a) are within the range. Therefore, the motor in Fig. 8(a) is identified as a normal motor. In Fig. 8(b), the waveform area difference ratio is 31.1%, which exceeds the standard range and is identified as the motor abnormality of the stator coil layer's short circuit.

Fig. 7. (Color online) Photographs of (a) U–V line resistance measurement results of normal stator, (b) U–W line resistance measurement results of normal stator, (c) U–V line resistance measurement results of abnormal stator, and (d) U–W line resistance measurement results of abnormal stator.

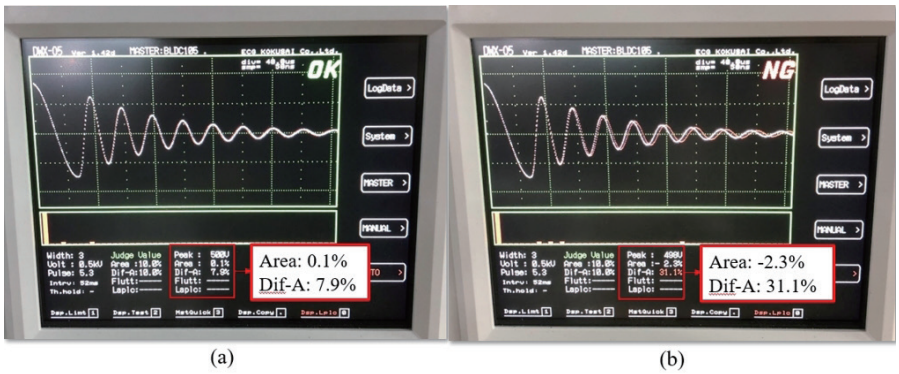

Fig. 8. (Color online) Photographs of layer short circuit measurement results of (a) normal and (b) abnormal stator coils.

2.2.3 Bearing faults

There are many possibilities of bearing damage, such as abnormal assembly dimensions, which induce wear and extrusion, very high operating temperature, incorrect bearing material specifications selected, and foreign matter infiltration. In Fig. 9, (a) is a normal bearing, (b) is a bearing with poor lubrication, (c) is a bearing with a 3 mm inner ring damage shown in the red circle, and (d) is the extrusion damage to the ball (red circle) resulting from the damaged cover of the ball bearing.

3. Proposed Methods

CNN is a type of supervised learning. In recent years, it has been widely used in signal processing and image classification, such as face recognition, imaging medicine, and fault diagnosis. The model design of CNN varies with the characteristic structure of data and its composition architecture. The structure of CNN consists of several convolutions, pooling, and fully connected layers. An activation function is appropriately added to each node in the layers. The CNN architecture proposed in this paper is shown in Fig. 10. The measured signals go through an input layer, two convolution layers with tanh activation function, a pooling layer, and a fully connected layer to identify the motor fault class.

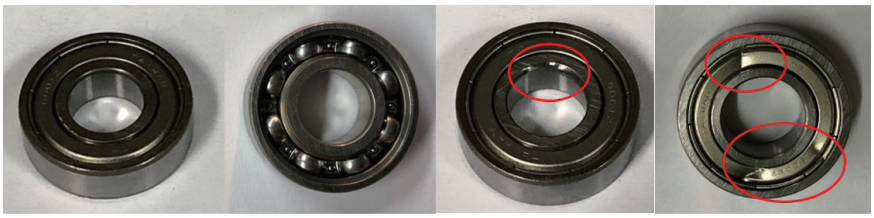

(a) (b) (c) (d)

Fig. 9. (Color online) Photographs of (a) normal bearing, (b) bearing with poor lubrication, (c) bearing with inner ring damage, and (d) bearing with ball damage.

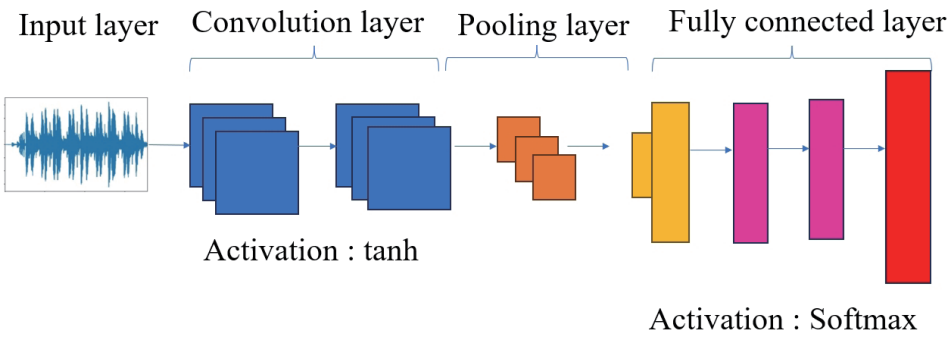

Fig. 10. (Color online) CNN architecture diagram.

3.1 1D-CNN

The CNN can be divided into three types: 1D, 2D, and 3D. These dimensions refer to the dimensions of the feature detector sliding between the data. 1D-CNN is often used in processing time series data and natural language processing. 2D-CNN is often used in computer vision and image processing. 3D-CNN is often used in the medical field and video processing. In this study, 1D-CNN is the model architecture. Figure 11 shows the basic principle of 1D-CNN, that is, to extract and combine the features in the sequence data through convolution operations and nonlinear activation functions. 1D-CNN performs convolution operations for the input sequence by sliding the convolution kernel, calculating a new feature map, and adjusting the convolution kernel size to capture the features of different scales.

By applying several convolution kernels to the input time series data, 1D-CNN can capture different local patterns and extract high-level features. The main steps are described below.

Step 1: Use the original time series data as input data for the model.

Step 2: Perform convolution operations on the input data and generate a new feature map by sliding the convolution kernel.

Step 3: Reduce the dimensions of the feature map and extract data by reducing sampling operations to prevent overfitting. Common pooling methods include max pooling and average pooling.

Step 4: Include the flatten, connection, and output layers. They are responsible for converting the pooling layer into vectors and performing tasks such as classification or regression through the fully connected layer. The fully connected layer is called the dense layer in TensorFlow.

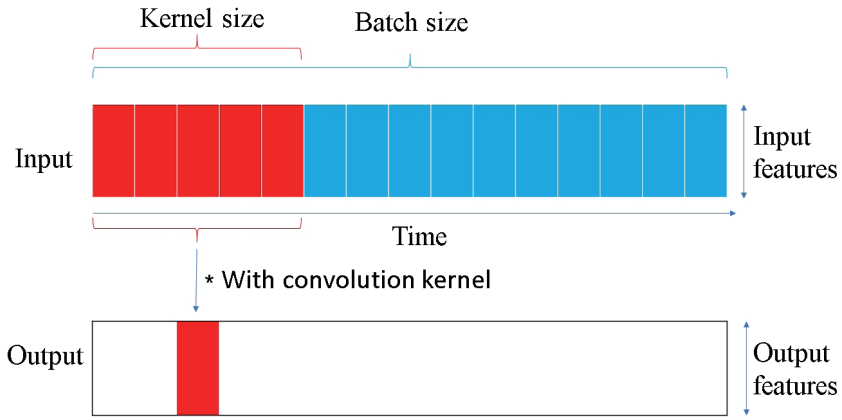

Fig. 11. (Color online) Schematic diagram of 1D convolutional layer extracting features.

3.2 Convolution layer

The main task of the convolution layer in CNN is feature capture. The convolution kernels or filters of different sizes perform convolution operations. The spatial filtering concept performs the image feature extraction or feature enhancement. The size of the convolution kernel affects the performance of feature detection. An overly small convolution kernel results in poor recognition performance, whereas an overly large convolution kernel is time-consuming and expensive. In this study, a 3 × 1 filter was used for the convolution operation of 7 × 1 data with a stride of one until all pixels of the original input image were completed by the masking operation (inner product). The feature map can be obtained. Figure 12 shows the schematic diagram of the convolution operation.

The 1D convolution layer uses the tanh (hyperbolic tangent) activation function. As shown in Eq. (1), x is the value of the input data and y is the output value calculated using the tanh function. The tanh function takes the actual value, normalized into the interval between −1 and 1. The output of the tanh function is centered on zero because the interval is between −1 and 1. The function is shown in Fig. 13.

$$y = f(x) = \tanh(x) = \frac{e^{x} - e^{-x}}{e^{x} + e^{-x}} = \frac{1 - e^{-2x}}{1 + e^{-2x}} \in (-1,1) \tag{1}$$

3.3 Pooling layer

An extracted feature image is obtained after the data passes through the convolution layer. To reduce the size of the features and maintain the feature invariance, a pooling layer is added after extracting the features using convolution. This reduces the operational complexity of the network and maintains consistent features of the image. The common pooling layer methods are divided into Max pooling and Average pooling. As shown in Eq. (2), R is the pooling filter and $R_{(ixj)}$ is the specification size of the pooling filter, which means that R is a matrix with i columns

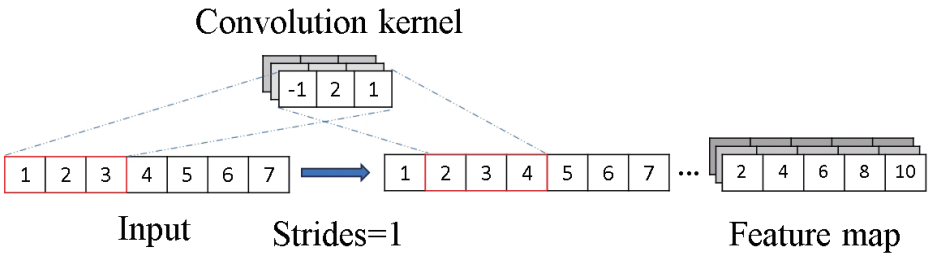

Fig. 12. (Color online) Schematic diagram of convolution operation.

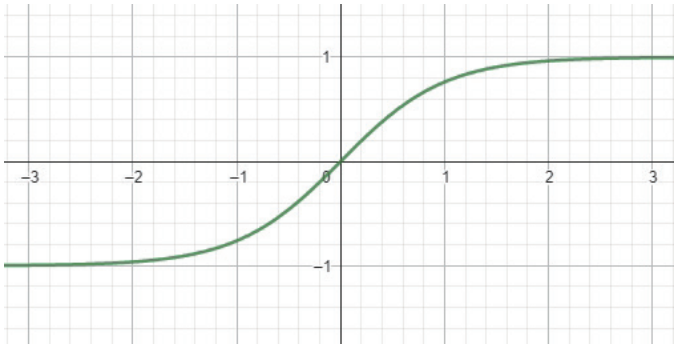

Fig. 13. (Color online) Graph of tanh function.

and j rows. k is the k-th feature map and p and q respectively denote the p-th column and q-th row in the matrix. X is the feature extracted from the feature map by the pooling filter; thus, $X_{k(p,q)}$ refers to the feature of the p-th column and q-th row extracted from the k-th feature map by the pooling filter. $y_{k(ixj)}$ is the output value obtained by the selected operation method.

The Max pooling operation method can be expressed as

$$y_{k(ixj)} = \max_{(p,q)\in R_{(ixj)}} X_{k(p,q)}. \tag{2}$$

The Average pooling operation method can be expressed as

$$y_{k(ixj)} = \frac{1}{\left|R_{(ixj)}\right|} \sum_{(p,q)\in R_{(ixj)}} X_{k(p,q)}. \tag{3}$$

Figure 14 demonstrates the operation mode of the pooling layer. Max pooling can be obtained by taking the maximum value in unit of one color block. The Average pooling method is similar to Max pooling, where Average pooling is calculated in unit of one color block. The Max pooling operation is adopted in this paper.

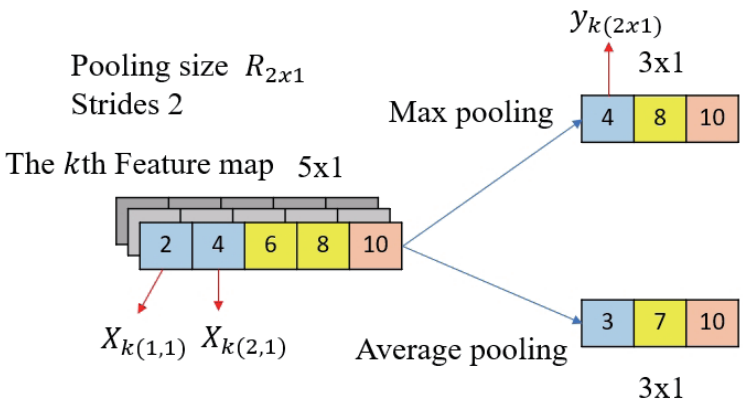

Fig. 14. (Color online) Schematic diagram of pooling layer operation.

3.4 Fully connected layer

The fully connected layer consists of three structures: flatten, dense, and output layers. It is in the neural network model at the end of CNN. Its main function is to convert the eigenmatrix exported from the convolution and pooling layers into a 1D vector through the flatten layer. Afterward, the error between the input and the output is adjusted by adjusting the weight and backpropagation in the dense layer before classification. The results are then displayed in the output layer. Figure 15 shows the composition diagram of the fully connected layer.

In the fully connected layer, the *Softmax* activation function for multi-class classification problems is used in this paper. If there are N classes to be predicted, *Softmaxx* forces the sum of all N output values in the neural network to be 1. Therefore, the output value represents the probability of occurrence of each N class as the prediction result. As shown in Eq. (4), N is the total number of classes, yi is the output value of the i-th class, $\sum_{j=1}^{N} e^{yj}$ is the sum of N output values, and the total value is 1. $Softmax(y)_i$ denotes the probability distribution between 0 and 1 of the output value of the i-th class.

$$Softmax(y)_i = \frac{e^{yi}}{\sum_{j=1}^{N} e^{yj}} \in [0,1] \tag{4}$$

4. Experimental Results

4.1 Motor fault measurement signal

Various motor vibration signals captured by the vibration spectrum analyzer are shown in Fig. 16. The x-axis is time (s) and the y-axis is vibration unit (G). The measurement settings are as follows: the bandwidth is 1578.5 Hz, the number of analysis items is 51200, and the data capture time is 32.4 s. Figure 16(a) represents the vibration measurement signals of a normal motor (Class A), and Figs. 16(b)–16(l) represent the vibration measurement signals of 11 motor

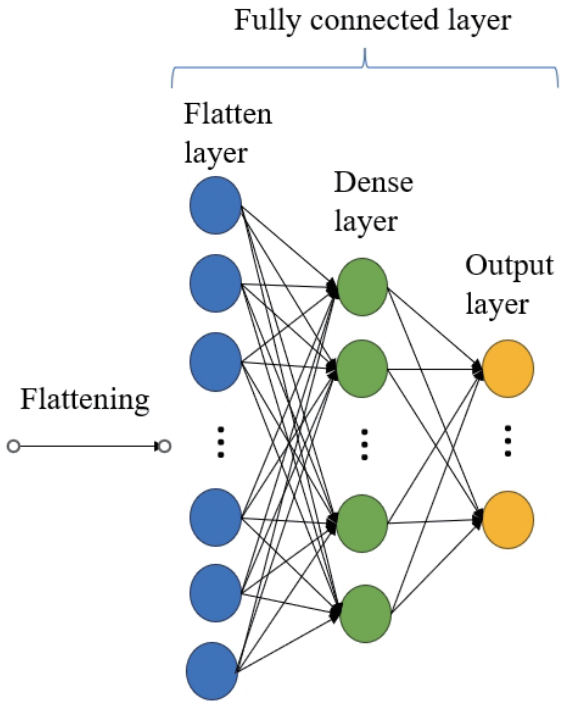

Fig. 15. (Color online) Schematic diagram of fully connected layer architecture.

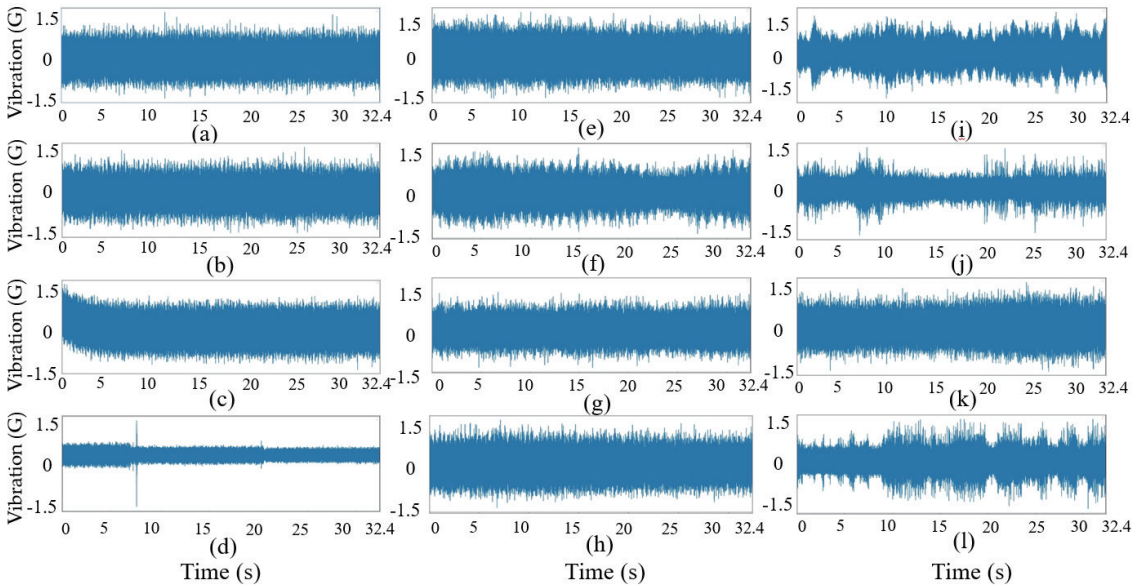

Fig. 16. (Color online) Vibration measurement signal diagram of (a) normal motor (Class A) and (b to l) 11 types of motor fault (Classes B–L).

fault types (Classes B to L). It can be seen that each type of motor signal has its features. The identification model built using the proposed method is used for feature extraction and recognition.

4.2 1D-CNN fault identification results

As shown in Fig. 17, the 1D-CNN recognition model used in this study has two convolution layers, the activation function is tanh, and there is one pooling layer. The pooling layer filter uses Max pooling, and the fully connected layer has one flatten layer, two dense layers, and one output layer. The activation function of the second dense layer is *Softmax*. Table 2 shows the parameters used in each layer and a brief introduction, with the final parameters using a filter size of 50 and a kernel size of 20. The model building environment is Python 3.7.16, the Jupyter Notebook version is 6.5.5, and the TensorFlow version is TensorFlow-gpu2.3. The test environment consists of Intel(R) Core™ i7-8750H CPU @ 2.20 GHz processor, Nvidia GeForce RTX 2060 display adapter, and Windows 10 64-bit operating system.

The motors are divided into 12 classes, namely, normal motor (Class A) and 11 fault types (Classes B to L). In this study, the data enhancement method was adopted, and 49080 vibration data were generated during the motor test. The train and test split contain 34356 and 14724 data items, respectively. The ratio of the number of training data to the number of testing data is 7:3. The simulation results are shown in Table 3. The accuracy of recognition using 1D-CNN is the highest at 99.7%, followed by 2D-CNN with an accuracy of 96.1%. The training and learning accuracy of 1D-CNN is 99.9%, and that of 2D-CNN is only 97.1%. In contrast, ENN had the lowest recognition accuracy of 95% and learning accuracy of 90%.

In this paper, the motor fault recognition results are presented in a confusion matrix. Figure 18 shows that the *x*-axis is the predicted fault type and the *y*-axis is is the actual fault type. The white and red grids in the confusion matrix represent the numbers of correct and incorrect recognitions, respectively. Taking Class H in Fig. 18 as an example, among the 1279 testing data, the proposed method identified 1278 data as Class H, and only one data was misidentified as Class D. Therefore, the recognition rate of Class H was 99.9%. Similarly, the recognition rate of the proposed method for Classes A, C, E, I, and L was 100%. Finally, the white grid values were added up and divided by the sum of the white and red grid values, and the total recognition accuracy was 99.7%.

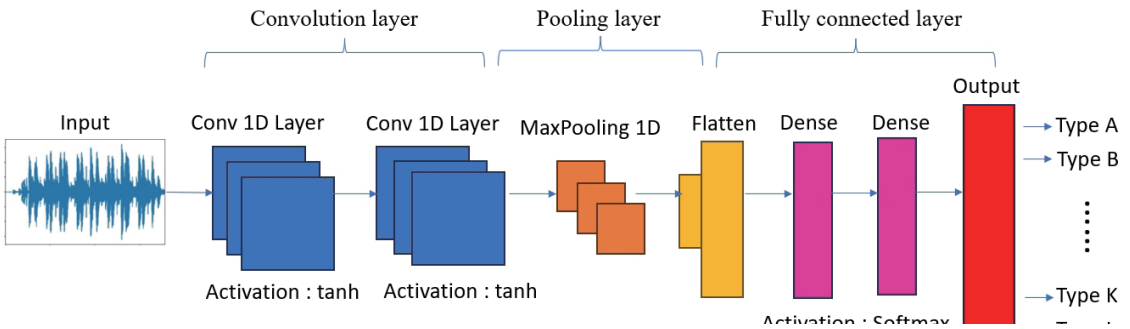

Fig. 17. (Color online) 1D-CNN architecture diagram.

Table 2
Parameters of each layer in convolutional neural network.

Layer	Number	Parameters
Conv1D	2	Filter = 50, kernel size = 20, activation function = tanh.
Pooling1D	1	Max pooling, pool size = 2.
Flatten	1	
Dense	1	Units = 30.
Dense	1	Units = 12, activation function = *Softmax*.

Table 3
Comparison of 1D-CNN, 2D-CNN, and ENN recognition results.

Detection method	Epoch	Training accuracy (%)	Learning accuracy (%)	Ranking
1D-CNN	50	99.9	99.7	1
2D-CNN	50	97.1	96.1	2
ENN	50	95	90	3

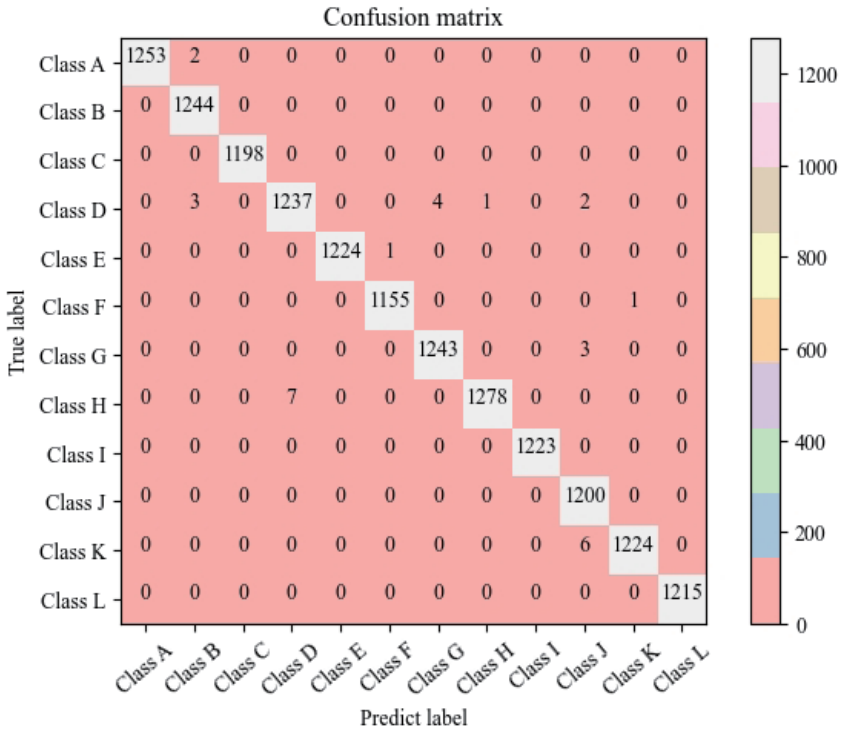

Fig. 18. (Color online) 1D-CNN confusion matrix.

5. Conclusion

In this study, we utilized 1D-CNN to develop a PMSM fault diagnosis system, aiming at multiple common PMSM fault types in practice. Fault diagnosis and identification were performed by measuring the time domain signals of motor vibration using the proposed 1D-CNN method. Experimental results showed that the recognition accuracy of the proposed

method is 99.7%. The time and instability in determining the cause of motor abnormality can be reduced effectively. The external factor that PMSM should be equipped with a driver is eliminated, making the practical application more convenient. In the future, a complete fault-type database will be built and continuously updated to reduce the possibility of misjudgment. The proposed method can be extended to other motor-related fields to develop fault diagnosis and identification systems for various motor types, such as servo motors, generators, electric vehicle motors, and wind power generation systems.

References

1 Y.-S. Jeong, S.-K. Sul, S. Schulz, and N. R. Patel: IEEE Trans. Ind. Appl. **24** (2005) 46. https://doi.org/10.1109/TIA.2004.840947
2 D. M. Ionel and M. Popescu: IEEE Trans. Ind. Appl. **46** (2010) 2424. https://doi.org/10.1109/TIA.2010.2073671
3 K.-Y. Chen, C.-C. Wang, A.-M. Chao, Y. Kang, and M.-H. Chu: J. Chung Yuan Christian University of Taiwan. **33** (2005) 329. https://doi.org/10.6358/JCYU.200509.0329
4 Z.-F. Wang, J.-Z. Yang, H.-P. Ye, and W. Zhou: Proc. 2014 IEEE Transportation Electrification Conf. and Expo, ITEC Asia-Pacific. (IEEE, 2014) 1–5. https://doi.org/10.1109/ITEC-AP.2014.6940870
5 A. Dineva, A. Mosavi, M. Gyimesi, and I. Vajda: Appl. Sci. **9** (2019) 5086. https://doi.org/10.3390/app9235086
6 J. Wang, Y. Peng, W. Qiao, and J.-L. Hudgins: IEEE Trans. Ind. Appl. **53** (2017) 3029. https://doi.org/10.1109/TIA.2017.2650142
7 K.-J. Kang, J.-Y. Song, C.-H. Kang, and S.-J. Sung: IEEE Trans. Ind. Electron. **64** (2017) 7191. https://doi.org/10.1109/TIE.2017.2686376
8 J. Hur, J. W. Reu, B. W. Kim, and G. H. Kang: IEEE Trans. Ind. Appl. **47** (2011) 1300. https://doi.org/10.1109/TIA.2011.2128850
9 B. Ebrahimi, M. J. Roshtkhari, J. Faiz, and S. V. Khatami: IEEE Trans. Ind. Electron. **61** (2014) 2041. https://doi.org/10.1109/TIE.2013.2263777
10 C. Bruzzese: IEEE Trans. Ind. Electron. **61** (2014) 4206. https://doi.org/10.1109/TIE.2013.2284554
11 B. Muruganatham, M. A. Sanjith, B. Krishnakumar, and S. Murty: Mech. Syst. Signal Process. **35** (2013) 150. https://doi.org/10.1016/j.ymssp.2012.08.019
12 D. S. Chandra and Y. S. Rao: J. Fail. Anal. Prev. **19** (2019) 1144. https://doi.org/10.1007/s11668-019-00712-z
13 H. Guesmi, S. B. Salem, and K. Bacha: Comput. Electr. Eng. **41** (2015) 226. https://doi.org/10.1016/j.compeleceng.2014.10.015
14 S.-R. Huang, K.-H. Huang, K.-H. Chao, and W.-T. Chiang: Comput. Electr. Eng. **54** (2016) 195. https://doi.org/10.1016/j.compeleceng.2016.01.028
15 N. M. Athif, S. Febriyanti, and K.N. Ramadhan: J. Ilm. Penelit. dan Pembelajaran Inform. **8** (2023) 281. https://doi.org/10.29100/jipi.v8i1.3324
16 M.-H. Ding, Y.-P. Ding, Y.-Q. Peng, and J.-X. Cao: IEEE Geosci. Remote Sens. Lett. **20** (2023) 3505305. https://doi.org/10.1109/LGRS.2023.3282700
17 Z. Meng, W. Cao, D.-Y. Sun, Q. Li, W.-X. Ma, and F.-J. Fan: Adv. Eng. Inf. **54** (2022) 101797. https://doi.org/10.1016/j.aei.2022.101797
18 S.-W. Xu, H.-T. Ru, D.-C. Li, P.-L. Shui, and X. Jian: IEEE Trans. Geosci. Remote Sens. **61** (2023) 5101311. https://doi.org/10.1109/TGRS.2023.3240693
19 Y.-F. Gu, Y.-J. Zhang, M.-R. Yang, and C.-S. Li: Appl. Sci. **13** (2023) 4192. https://doi.org/10.3390/app13074192
20 S.-Q. Zhou, L.-P. Lin, C. Chen, W.-B. Pan, and X.-C. Lou: Comput. Intell. Neurosci. **2022** (2022) 9231305. https://doi.org/10.1155/2022/9231305
21 H. Özcan, O. C. Devecioglu, T. Ince, L. Eren, and M. Askar: Electr. Eng. **104** (2022) 435. https://doi.org/10.1007/s00202-021-01309-2
22 R. F. Ribeiro Jr., I. Methodoly, M. Campos, C. Teixeira, L. Silva, and G. Gomes: Measurement **190** (2022) 110759. https://doi.org/10.1016/j.measurement.2022.110759
23 G-TECH Instruments Inc.: https://www.g-tech-inst.com/products_detail/202102170026.html?lang=eng (accessed May 2024).
24 International Organization for Standardization: https://www.iso.org/obp/ui/#iso:std:iso:2768:-2:ed-1:v1:en (accessed May 2024).

25 F.W. Bell Inc.: https://www.transcat.com/media/pdf/FWBell6010.pdf (accessed May 2024).
26 HIOKI E.E. CORPORATION: https://www.hioki.com/global/products/resistance-meters/resistance/id_5998 (accessed May 2024).
27 Public Construction Committee of the Executive Yuan of the Republic of China : https://ws.pcc.gov.tw/001/upload/old/oldupload/upload/article/Electromechanical_device_2_1.pdf (accessed May 2024).
28 ECG KOKUSAI Co., Ltd.: http://www.ecginc.co.jp/english/coil01.html (accessed May 2024).